Annihilation of craters: Molecular dynamic simulations on a silver surface

K. O. E. Henriksson[*]

Royal Institute of Technology, Department of Reactor Physics, S-10691 Stockholm, Sweden

K. Nordlund and J. Keinonen

Accelerator Laboratory, P.O. Box 43, FI-00014 University of Helsinki, Finland

The ability of silver cluster ions containing 13 atoms to fill in a preexisting crater with a radius of about 28 Å on a silver (001) target has been investigated using molecular dynamics simulations and the molecular-dynamics–Monte Carlo corrected effective medium potential. The largest lateral distance r between crater and ion was about three times the radius of the preexisting crater, namely, 75 Å. The results reveal that when $r < 20$ Å and $r > 60$ Å the preexisting crater is partially filled in, and for other distances there is a net growth of the crater. The lattice damage created by the cluster ions, the total sputtering yield, the cluster sputtering yield, and simulated transmission electron microscopy images of the irradiated targets are also presented.

I. INTRODUCTION

Experimental[1–4] and theoretical[5–11] studies of crater formation on dense metals such as copper, silver, and gold irradiated with heavy energetic ions show that craters—not unlike scaled down versions of meteorite craters—can form on these targets. Only a small number of these studies have focused on the modification of craters by subsequent ion impacts.[2,3]

The modifications by an ion of a preexisting crater fall into two main categories: (i) removal of atoms at the crater surface and (ii) insertion of atoms onto the crater surface. The net modification is given by the sum of these changes, and is in one extreme the birth of a larger crater, and in the other extreme the formation of a second crater. For a given combination of target and ion species, ion energy, and target temperature the most obvious parameter which influences the outcome is the lateral distance r between the preexisting crater and the incident ion, measured on the plane of the pristine surface.

An example of detailed analysis of the alteration of preexisting or initial craters by ions can be found in the study by Donnelly and Birtcher.[3] In this case gold films were irradiated with xenon ions with energies in the range 50–400 keV. It was found that ions are able to fill in or annihilate small craters with an average radius of $R = 22$ Å, provided they impact inside a circle with radius 50 Å $\approx 2.3R$ centered on the crater. By inspection of high-speed video of the irradiation events the authors were able to explain the annihilation of craters to be caused by flow of molten material. The melt was formed in surface-near spikes, in a similar fashion as illustrated by the molecular dynamics results of Ghaly and Averback[5] of 10 and 20 keV self-irradiation of gold.

In the present study the efficiency of Ag_{13} cluster ion impacts to partly or completely annihilate a preexisting crater on (001) silver is investigated using molecular dynamics simulations. Cluster ions were selected, since the relative uncertainty in the sputtering yield—and therefore the volume of the formed craters—has been found to decrease with increasing number of atoms in the bombarding particle.[6,12] The 20 keV ion energy is high enough to give rise to craters

without causing lattice damage reaching far into the bulk. Silver was chosen over gold, since most of the other studies mentioned above have focused almost entirely on gold. The crater annihilation efficiency is systematically investigated as a function of the lateral distance between the preexisting crater—which was made in the zeroth impact simulation—and the normally incident ion. Results on lattice damage, sputtering yield, and simulated transmission electron microscopy (TEM) images are also presented.

II. COMPUTATIONAL METHODS

A. The basis of molecular dynamics simulations

Newtonian—or classical—molecular dynamics simulations (MDS) is a widely used method to investigate the behavior of a system of atoms according to a given interaction model. The time evolution is completely deterministic. The MDS rely on the Born-Oppenheimer approximation, according to which the evolution of the electronic and nuclear systems—represented by the valence electrons of the atoms and the remaining heavy ionic cores, respectively—occur on vastly different time scales. This means that the (valence) electrons can be assumed to "instantenously" reach the ground state of any given new configuration of the ionic cores. By this approximation the evolution of the system is completely determined by the motion of the cores, hereafter referred to as "atoms."

In the present study the motion of the atoms was obtained by using the Gear fifth order corrector-predictor algorithm.[13] For the integration an adaptive time step was used,[14] thus speeding up the calculations when the highest atomic kinetic energy in the system is low. For efficient execution of the code, linked lists[15] and a two-dimensional domain decomposition of the simulation cell for parallel computers was used.

B. Interatomic potential

The corrected effective medium (CEM) potential tailored for molecular dynamics (MD) and Monte Carlo (MC) calculations—abbreviated MD/MC-CEM—was used for the

present molecular dynamics simulations (MDS). See Refs. 16–20 for the complete description of the CEM and MD/MC-CEM potentials. The form used in the present calculations is based on the work by Kelchner *et al.*[21] The MD/MC-CEM potential does not rely on empirical inputs to the same extent as the embedded atom method potential (EAM),[22–26] which also is an effective-medium potential. The MD/MC-CEM potential is fitted to both bulk and dimer energies, and therefore gives a better description of, e.g., surface phenomena, such as the energy of low-index surfaces,[20] than the EAM potential.

The MD/MC-CEM is based on the CEM potential, which gives the total energy of a monoatomic solid as

$$E(N) = \sum_{i=1}^{N} E_J(n_{h,i}) + \frac{1}{2}\sum_{i=1}^{N}\sum_{j=1,i\neq j}^{N} V_{ij} + \sum_{i=1}^{N} G_i, \quad (1)$$

where $E_J(n_{h,i})$ is the embedding energy of atom i, V_{ij} is the total Coulomb interaction energy of atoms i and j (electron-electron, electron-nuclear, and nuclear-nuclear), and G_i is a correction for the kinetic exchange-correlation energy difference between the inhomogeneous electron gas in the real bulk and the jellium system.[27] The jellium density is

$$n_{h,i} = \frac{1}{2Z_i}\sum_{j=1,j\neq i}^{N}\int dV n(\mathbf{r}-\mathbf{R}_i)n(\mathbf{r}-\mathbf{R}_j), \quad (2)$$

where $n(\mathbf{r}-\mathbf{R}_i)$ is the atomic electron density from Hartree-Fock calculations. The nuclei are at positions $\mathbf{R}_i, \mathbf{R}_j$. The Coulomb energy is

$$V_{ij} = \int dV_1 dV_2 |\mathbf{r}_1 - \mathbf{r}_2|^{-1}[n(\mathbf{r}_1 - \mathbf{R}_i) - Z_i\delta(\mathbf{r}_1 - \mathbf{R}_i)]$$
$$\times [n(\mathbf{r}_2 - \mathbf{R}_j) - Z_j\delta(\mathbf{r}_2 - \mathbf{R}_j)] \quad (3)$$

(see Ref. 17). In the MD/MC-CEM formalism suitable for Monte Carlo and molecular dynamics calculations, the combination $E_J(n_{h,i}) + G_i$ is replaced by $F_J(n_{h,i})$ (Refs. 20 and 27). This is an approximation, since the functional G_i has been replaced by a function.

The unknown embedding function can be determined from the relation

$$\sum_{i=1}^{N} F_J(n_{h,i}) = E(N) - \frac{1}{2}\sum_{i=1}^{N}\sum_{j=1,i\neq j}^{N} V_{ij}, \quad (4)$$

provided the cohesive energy $E(N)$ is known. To get embedding energies that can give a good description of both low- and high-coordination bonding, the following two cases are considered. For a monoatomic solid one has

$$F_J^b(n_{h,i}) = NE^b - \frac{1}{2}\sum_{j=1,i\neq j}^{N} V_{ij}, \quad (5)$$

and for a homonuclear dimer

$$F_J^d = \frac{1}{2}[E_c - V(R)]. \quad (6)$$

The bulk atomic energies E^b can be obtained for different lattice parameters from linear muffin tin orbital (LMTO) cal-

culations (after shifting to achieve agreement with experimental cohesive energies and lattice parameters),[21,27] and the dimer atomic energies E_c can be obtained from Morse curve fitting to experimental data.[21] The full curve for the embedding energy is then obtained by suitable interpolation of low and high electron density cases.

From this brief overview it is clear that the inclusion of dimer data makes the MD/MC-CEM potential better suited for systems containing a significant amount of (small) clusters and structures with low coordination, such as surfaces. As a matter of fact, Wucher and Garrison[28] have shown that the MD/MC-CEM gives much better binding energy of silver dimers and trimers than EAM, when comparing to experimental and *ab initio* values. Also, a study of sputtering of gold by xenon ion impacts over a broad energy range shows that at 5–100 keV the MD/MC-CEM potential gives a more accurate (closer to experimental) description of the sputtering yield than the EAM potential.[10] The latter potential gave sputtering yields Y_{EAM} which were larger than the experimental ones Y_{exp} by a factor $f = Y_{EAM}/Y_{exp} = 1.5 - 6.2$, whereas the MD/MC-CEM had $f = Y_{MD/MC-CEM}/Y_{exp} = 0.5 - 1.5$.

The MD/MC-CEM potential does not provide data for atomic distances approaching $r_{ij} = 0$, which are relevant in high-energy collisions. For these distances the universal interatomic potential by Ziegler, Biersack and Littmark[29] was used. This potential is given as $V_{ZBL}(r_{ij}) = \Phi_U(x)Z_iZ_je^2/r_{ij}$, with $x = r_{ij}/a_U$, $a_U = 0.8854a_0/(Z_i^{0.23} + Z_j^{0.23})$, a_0 being the Bohr radius and $\Phi_U(x) = \sum_{i=1}^{4} a_i e^{-b_i x}$ is the universal screening function. The values for a_i, b_i can be found in Ref. 29. The uncertainty in the potential is $\lesssim 20\%$.

C. Electronic stopping

Electrons are not explicitly treated in Newtonian MDS. This becomes problematic at high ion energies, when energy transfer from the ion to the target atoms via ion-electron and electron-electron collisions (and electron excitations in the incident atom and the target) becomes increasingly important. This "electronic stopping" is usually handled with a "friction" term in the equations of motion: the path length traveled by an atom which is to experience energy loss due to electronic interactions is multiplied by the velocity-dependent electronic stopping, and the result is subtracted from the atom energy. In the present simulations the electronic stopping function of Ziegler, Biersack, and Littmark[29] was applied to all atoms having an energy ≥ 5 eV.

D. Simulation for the development of the initial crater and the ion-crater interactions

The methodology used to make the initial or preexisting crater and handle the other impact events has been described in a previous article.[11] Here only the most important details are recapitulated.

The simulation of the birth of the initial crater was carried out by letting a Ag_{13} cluster with a total energy of 20 keV impact on a silver target with the dimensions $L_x = L_y \approx 297$ Å and $L_z = 148$ Å. The target initially had a tempera-

ture of 0 K, and was heated by the incident particle. The lattice parameter was $a=4.12$ Å, corresponding to a temperature of 300 K. This temperature was achieved in a relaxation run after the cascade had ended, see below. The number of atoms in the bulk was $4 \times 72 \times 72 \times 36 = 746\ 496$.

The cluster projectile was made by cutting out all the 12 nearest neighbors of an atom in a lattice at 300 K. No relaxation was carried out on the cluster. The cluster was randomly rotated and placed at about 25 Å above the surface. Periodic boundary conditions were used in the x and y directions. To remove the lower open z boundary, all the atoms in a 5 Å thick region at the boundary were kept fixed at all times. In this way only one true open surface remained.

To model the dissipation of heat and pressure into the medium surrounding the cascade, the Berendsen temperature control method[30] was used: The atoms in a $2a$ thick region directly adjacent to the layer of fixed atoms at the bottom of the simulation cell—and the atoms at all the periodic boundaries—were subjected to velocity scaling. In this way the temperature in these regions was controlled towards 300 K.

The simulation was ended at 50 ps after ion impact. At this time the system had reached thermal equilibrium, but with a temperature not close to 300 K, since the target initially was at 0 K. Therefore the system was run for an additional 2 ps in order to ensure a homogeneous temperature of 300 K everywhere. After this all sputtered atoms were removed. The resulting crater was clearly hemispherical.

For the simulations of cluster ions impacting on the preexisting crater the same conditions for temperature scaling, atom fixing, and cluster position as above were used. However, the simulation time was extended to 80 ps to ensure a long and complete relaxation.

The impact points for the 13-atom silver clusters were selected randomly inside a circular area with the radius 75 Å centered on the preexisting crater. To reduce the total number of simulations the circular area was divided into annuli with thickness $d=5$ Å. The distance from the initial crater to any annulus—the "binned" lateral distance—was

$$r_i = \left(i + \frac{1}{2}\right)d, \tag{7}$$

with $i=0,\dots,14$, resulting in $\min(r_i)=0.5d=2.5$ Å and $\max(r_i)=14.5d=72.5$ Å. In order to keep the number of simulations to a minimum, an impact probability of $p = N_i/A_i \times \pi d^2 = 0.49$ was selected. This quantity is not important *per se*, it is merely a tool to find a suitable value for N_i, the number of impacting ions per annulus. Since the area of each annulus is

$$A_i = \pi[(i+1)^2 - i^2]d^2 = \pi(2i+1)d^2, \tag{8}$$

this gives

$$N_i = p(2i+1) \approx i \tag{9}$$

clusters per annulus, and a total of 105 impact simulations (not counting the one producing the initial crater).

Before any simulation started, the substrate was shifted in the x and y directions, such that the cluster always impacted at $(x,y)=(0,0)$, and the preexisting crater was located at $(r \cos \theta, r \sin \theta)$. The "direct" lateral distance $r \in [0,75]$ Å and the angle $\theta \in [0,2\pi)$ were chosen randomly.

E. Analysis of crater annihilation

The initial and final positions of the atoms were analyzed for vacancy clusters. The largest clusters were identified as the excavated crater regions.

The vacancy analysis was carried out as follows. One of the fixed atoms at the bottom of the simulation cell was selected as a reference atom. A perfect lattice was then constructed using this atom, and overlaid on the existing damaged lattice. For each atom the smallest distance to any lattice point P was calculated. If this distance was less than 120% of half the nearest neighbor distance $r_{NN}=2.91$ Å, i.e., $r_c = r_{NN}/2 \times 1.20 = 1.7$ Å, then this atom was identified with the point P in the perfect lattice. At the end of the analysis, all unoccupied lattice points were labeled as vacancies.

In the general case the above vacancy analysis gave a system containing vacancy clusters V_n, with $n \geq 1$. In addition, the larger clusters, reminiscent of macroscopic craters, were sometimes decorated by small protrusions. Also, some isolated vacancy planes were found. In order to obtain a good estimate of the size of the "true" craters, i.e., the dense vacancy clusters, the superfluous separated and clustered vacancies had to be removed. For this purpose the following recipe was followed.

(1) All vacancies below the height of the pristine surface were obtained.

(2) The number N_{NN} of nearest neighboring (NN) vacancies for each vacancy i, i.e., all vacancies $j \neq i$ for which $|\mathbf{r}_i - \mathbf{r}_j| \leq r'_{NN}$, was calculated. Here $r'_{NN}=3.0$ Å is a little larger than the true distance $r_{NN}=2.91$ Å.

(3) The plane going through vacancy i and two of its nearest neighbors was constructed.

(4) The number N_{OOP} (OOP for out-of-plane) of nearest neighbors which were at a distance $d \geq 1.0$ Å (suitably large) from this plane was determined. The equation for the plane was established using the vacancy i and its two neighbors. Then the positions of all other neighbors of vacancy i were projected onto this plane, and the distance d between the projected point and the real position was calculated.

(5) If vacancy i had $N_{NN} \geq 3$ and $N_{OOP} \geq 1$ it was saved for further processing.

(6) All saved vacancies were investigated for clustering. The resulting distribution was dominated by one or two large vacancy clusters, and some smaller clusters. These smaller clusters usually contained much less than 100 vacancies, corresponding to $\leq 5\%$ of the size of the initial crater. These vacancy clusters were not connected to the crater regions, but instead spread out in the lattice below the craters.

In step (5), the criterion $N_{NN} \geq 3$ alone removes any isolated {110} plane, in which any vacancy has only two nearest neighbors. The combination of conditions is needed to remove isolated {100} and {111} planes, in which any vacancy has four and six NN, respectively, but none of them out of

the plane. In the case of two stacked low-index planes ({100}, {110}, {111}) surrounded by vacuum, it is true that any vacancy always has at least six NN, of which at least three NN are outside any of the planes formed by the other vacancies. The criteria in stage (5) therefore retains any combination of two stacked low-index planes. This clearly protects the interior of large vacancy groups from being punctured. Analysis with and without stages (2)–(5) were carried out for randomly selected simulations. In cases with initially smooth-surface vacancy clusters the number of final vacancies differed only by a very small amount.

After the vacancy analysis was completed, there remained only one or two vacancy clusters, representing a modified and/or completely new crater. The vacancy cluster intersecting the initial crater was called "old," and any second crater was called "new." The number of vacancies in the initial crater was N_i, and the corresponding numbers for the old and new craters are M_1 and M_2, respectively. Furthermore, the number of vacancies in the initial crater not present in the old crater was denoted N_r, and the number of vacancies added to the initial crater crater was denoted N_e ("e" for expansion). The total number of vacancies in the old crater then equals the number of vacancies in the initial crater minus the number of removed vacancies plus the number of added vacancies

$$M_1 = N_i - N_r + N_e. \quad (10)$$

It should be noted that the quantity N_r—the number of vacancies that have been removed from the initial crater due to the impact of the cluster ion—can be used as an intuitive measure of the filling-in of the hemispherical region of the initial crater. This is so, because the number N_e of added vacancies comprise not only vacancies added at the sides or bottom of the initial crater, but also vacancies in a possibly new crater connected to the old one. We also define the volume-relevant quantities $V_i = N_i \rho$ as the volume of the initial crater, $V_1 = M_1 \rho$ as the volume of the old crater, $V_2 = M_2 \rho$ as the volume of the new crater, if present, and $V_r = N_r \rho$ as the volume of the vacancies removed from the initial crater.

Using these concepts the following quantities were defined. The relative change in the size of the initial crater—the net growth factor—is

$$f = \frac{M_1 - N_i}{N_i} = \frac{-N_r + N_e}{N_i} = \frac{V_1 - V_i}{V_i}. \quad (11)$$

The relative change in total crater volume is

$$f_V = \frac{M_1 + M_2}{N_i} = \frac{V_1 + V_2}{V_i} = 1 + f + \frac{V_2}{V_i}. \quad (12)$$

The removal or annihilation factor is defined as

$$f_r = \frac{N_r}{N_i} = \frac{V_r}{V_i}. \quad (13)$$

The expansion factor is

$$f_e = \frac{N_e}{N_i} = \frac{M_1 - N_i + N_r}{N_i} = \frac{M_1 + N_r}{N_i} - 1 = \frac{V_1 + V_r}{V_i} - 1 = f + f_r. \quad (14)$$

The quantities f, f_V, f_r, f_e were obtained as a function of the binned and direct lateral distances r_i and r, respectively, between the cluster ion and the initial crater.

F. Dislocations

An arbitrary group of four simulations was investigated for dislocations at the end of the cascade. Before the analysis, the target was cooled from about 300 to 0 K during a time of 3 ps, and then kept at zero for an additional 2 ps.

Dislocations—and other defects—in a specified lattice can be obtained by using the centrosymmetry-parameter.[31,32] Let $\mathbf{D}_i$ and $\mathbf{D}_{i+Z/2}$ denote the distance vectors to all nearest neighbors (NN) of an atom A in the perfect lattice, such that $\mathbf{D}_i = -\mathbf{D}_{i+Z/2}$. Here Z is the coordination—the total number of NN—of A in the perfect lattice [$Z = 12$ for the Ag face-centered cubic (fcc) lattice]. Furthermore, let the distance vectors to the real neighboring atoms of A closest to the perfect neighbor be denoted by $\mathbf{d}_i$.

The centrosymmetry of atom A is now defined as

$$C_s = \sum_{i=1}^{Z/2} |\mathbf{d}_i + \mathbf{d}_{i+Z/2}|^2. \quad (15)$$

For an atom in the perfect lattice $\mathbf{D}_i = \mathbf{d}_i$, so that $C_s = 0$. A bulk atom with a missing neighbor has $C_s = a^2/2 \approx 8.5$ Å². For an atom in the (001) surface $C_s = 4 \times 2(a/2)^2 = 8(a/2)^2 = 33.9$ Å². Since $C_s \propto a^2$, we can easily convert the identification recipe by Kelchner et al.[31] for defects in gold ($a \approx 4.08$ Å) to those in silver ($a \approx 4.12$ Å): $C_s \approx 8.5$ Å² for intrinsic stacking faults, and $C_s \approx 2.1$ Å² for atoms halfway between face-centered cubic and hexagonally close-packed sites. A nearest-neighbor distance of $r'_{NN} = 1/2(r_{NN} + r_{2NN}) \approx 3.52$ Å was used in the calculations in order to include nearest neighbors with full certainty. Here $r_{NN} \approx 2.91$ Å, and $r_{2NN} = 4.12$ Å is the second nearest-neighbor distance.

G. Simulation of TEM images

In experiments the crater annihilation efficiency of the ions has been illustrated by transmission electron microscopy (TEM) images of the irradiated targets.[2,3] In these images unaffected surface areas are grey, craters are white, and deposited particles are black. The latter two are surrounded by fringes of opposite color.

In order to ascertain that present results of two connected craters can be distinguished from a single crater in an experimental situation some of the irradiated targets were TEM simulated. The TEMSIM package written by Kirkland[33] was used for these calculations. The experimental conditions of an electron beam with an energy of 300 keV, a 1000 nm underfocus, and a spherical aberration of 2.8 mm were used. However, the beam incidence was normal instead of 15° off-normal as in corresponding experiments.[3] The objective aperture was set to 10 mrad, after checking that other values
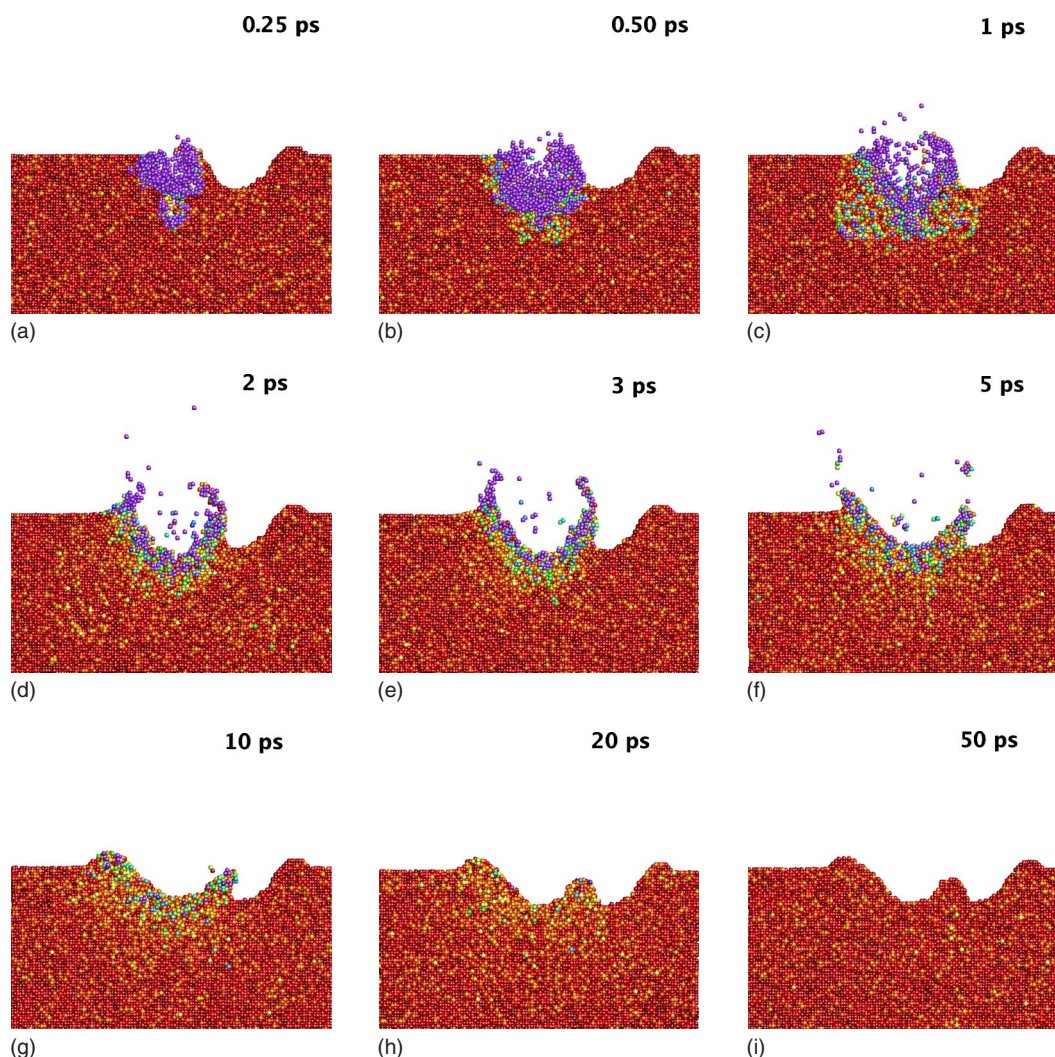
FIG. 1. (Color online) Cross sectional snapshots of a cascade induced by a cluster ion impacting at a lateral distance of $r=50$ Å from the initial crater. (a)–(c) The crater core is being formed by sputtering and ejection of material onto the surface. (d)–(f) The crater rim is created from surface atoms pushed aside by the cascade and sputtered material emitted with a polar angle so large it reattaches to the surface. (g) Some material is still being sputtered from the crater, which cools down during the next tens of picoseconds. (h) At 50 ps since ion impact the cascade is definitely over. Any changes to the crater after this time would be due to redeposition of material or thermal migration of adatoms or defects. The arbitrary color limits are the same for all images. The color indicate the kinetic energy (temperature) of the atoms. Red represents 39 meV (300 K), whereas blue represents 1.5 keV (12 million K). The latter corresponds to the kinetic energy per atom of the incident cluster ion.

varying with ±5 mrad did not produce significantly different images. The objective aperture was not displaced from the beam, but was located at $(x,y)=(0,0)$, so that bright-field images were obtained. Three different sample thicknesses were used: (i) $L_1=L_z/2=72$ Å, (ii) $L_2=132$ Å, and (iii) $L_3=L_z=148$ Å. Here L_z is the thickness in the z direction of the original simulation cell. The thickness L_2 was obtained by subtracting from L_z a slightly larger value than the total thickness of the layers containing fixed atoms and atoms whose velocities were scaled. These thinned samples were obtained by cutting away material from the open unirradiated bottom surface. All the samples were positioned so that the lowest atomic layers were at $z=0$.

III. RESULTS

A. Growth and annihilation

Before presentation of the results concerning the filling-in of the initial crater, it may be useful to illustrate how this comes about. The particular bombardment event used for this purpose is shown in Fig. 1. In this case the cluster ion is impacting at a distance of about 50 Å from the initial crater.

Due to large mass of the cluster ion (about 3600 a.m.u.) and the low energy of 1.5 keV per atom, its range is very short, resulting in a cascade close to the surface. The crater core—i.e., the initial vacancy cluster formed by the ion—develops during the first few picoseconds, as can be seen in parts (a)–(d) in the figure. The crater rim evolves at the same

time. This rim is being built up of surface atoms displaced onto the surface by the cascade, as can be seen in parts (c) and (d). In parts (e) and (f) a cluster is sputtered from the rim, which appears to be falling down to fill the adjacent initial crater. However, from parts (g) and (h) it is clear that this does not happen: instead the collapsing rim is retracted by the densification of the crater surface due to cooling. At 20 ps since ion impact the crater is more or less in its final form, but some relaxation and heat loss is still taking place. The initial crater is partly filled with displaced atoms, but there has not been any viscous flow into the crater.

Vacancy analysis of the initial crater showed that it was comprised of about $N_0 = 2320$ vacancies. Furthermore, the topmost circular layer of the cluster contained 289 vacancies. Using a surface density of $\sigma = 2/a^2$, with $a = 4.12$ Å, the radius of the top layer becomes $R_s = 27.9$ Å. The depth of the crater is $h = 26.8$ Å. Using N_0, the volume density $\rho = 4/a^3$, and the formula for the volume of a half-sphere we get a radius of about $R = 25.7$ Å. As a numerical measure of the deviation of the crater from a hemispherical shape we may use (i) $\sqrt{[2(R_s/R)^2 + (h/R)^2]/3} = 1.07$, (ii) the ratio 1.08 of half-ellipsoidal to half-spherical volumes, or any other reasonable quantity. These values show that the crater to a very good approximation is hemispherical. For later use, we define as the linear-size measure of the crater the weighted average $R \equiv (2R_s + h)/3 = 27.5$ Å.

The results for the quantities f, f_V, and f_r defined in Sec. II E are shown in Figs. 2–4. The (a) parts display the results with respect to the binned lateral distance between ion and crater and the (b) parts with respect to the real distance. The scatter along the vertical axis in the latter case, for a given set of similar distances, is brought about in part by the vacancy analysis method, and in part by the statistical fluctuations in the development of the individual cascades.

The plot of $f = (V_1 - V_i)/V_i$ in Fig. 2 shows that the initial crater with volume V_i is filled in ($V_1 < V_i$ and $f < 0$) when $r \lesssim 20$ Å and $r \gtrsim 55$ Å. The partial annihilation of the pre-existing crater in the latter case is easily understood as caused by the deposition of material excavated to make the new adjacent crater with volume V_2. However, the mechanisms at play in the former case $r \lesssim 20$ Å are not equally clear.

When the cluster ion impacts close to the preexisting crater the energized material is not as free to move about as when the ion impacts at a smooth surface. The displaced material is for most part trapped in the preexisting crater, which would give $V_1 \approx V_i$ and $f \approx 0$. To have $f < 0$ and $V_1 < V_i$ vacancies (or other defects) which decrease the crater volume must be created in the surrounding lattice.

For instance, the smallest f value for small distances r is -0.32 and occurs for $r \approx 8$ Å. The intial and final state of the atomic system in this case are illustrated in Fig. 5. It is easily seen that density-decreasing defects are present outside the crater in the lattice. Indeed, a closer look at the marked regions shows that single atomic planes with a normal (100) are missing between the crater and the bulklike lattice further down. In addition, the centrosymmetry analysis results presented below in Sec. III B and in Figs. 6 and 7 reveal the presence of stacking faults and dislocations under the old crater. From these facts the filling-in of the initial crater
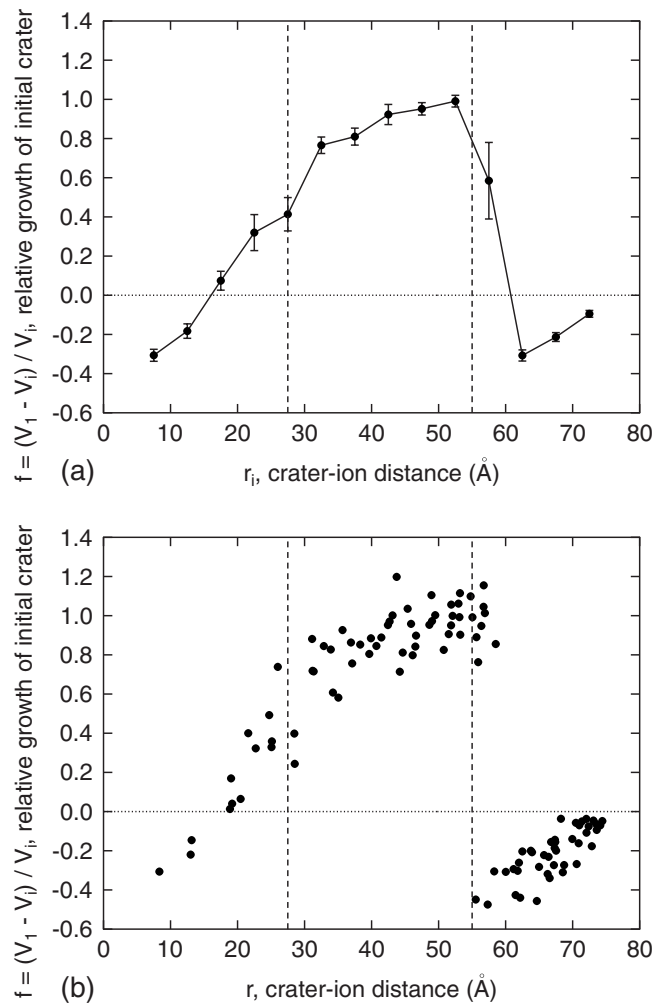

FIG. 2. Results for the growth fraction f, as a function of the (a) binned distance r_i and (b) the real distance r. The broken line is intended as a guide for the eye.

when the cluster ion impacts close to it can be understood in the following way. The cluster ion locally melts the bottom of the initial crater, displacing material up the crater walls and to a lesser extent out of the crater. When the cascade cools the lattice at the bottom of the crater is rebuilt, but not without defects. The volume-increasing (for the lattice, not the crater) defects makes the relaxed crater to have a smaller depth than before, giving $V_1 < V_i$ and $f < 0$.

When the ion-crater distance approaches 60 Å a new crater starts to form next to the old one. Since the new crater, with volume V_2, is not accounted for in the expression $f = (V_1 - V_i)/V_i$, this causes a discontinuity in the curve $f = f(r)$. From this distance onwards, one has pure filling of the old crater. The amount of annihilation decreases with increasing distance, from $f \approx -0.4$ at $r \approx 60$ Å to $f \approx 0$ at $r \approx 75$ Å, and would be zero for two craters infinitely separated.

The data for the relative change $f_V = (V_1 + V_2)/V_i$ in the total crater volume in Fig. 3 show that the total volume grows rapidly with the distance r. Already at $r \approx 40$ Å, which constitutes 70% of the radius of the initial crater, one has $f_V \approx 2$, which represents twice the volume of the initial cra-
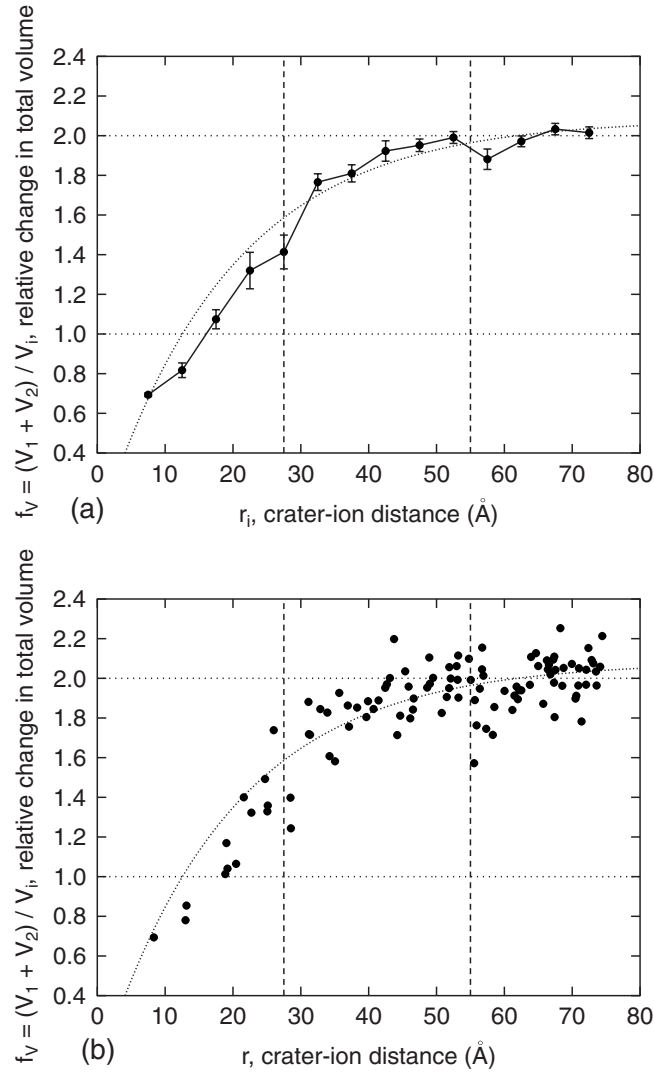
FIG. 3. Results for the volume fraction f_V, as a function of the (a) binned distance r_i and (b) the real distance r. The fit $f_V = a(1 - e^{-br})$ is also shown. The broken line is intended as a guide for the eye.
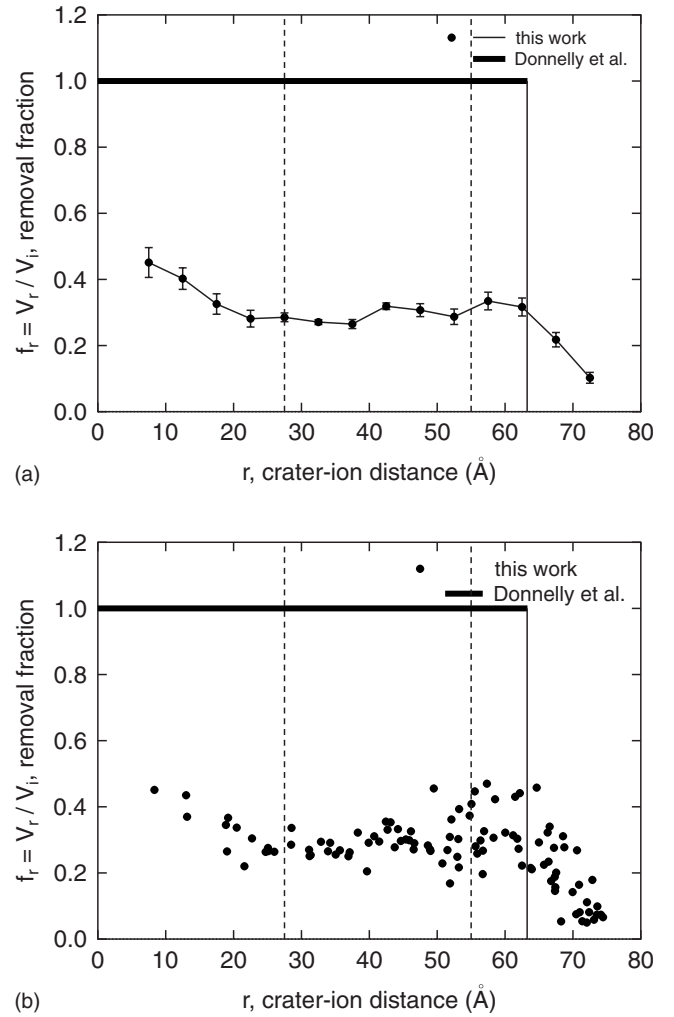

FIG. 4. Results for the removal fraction f_r, as a function of the (a) binned distance r_i and (b) the real distance r. The broken line is intended as a guide for the eye. This figure is discussed in Sec. IV A.

B. Dislocations

Relaxed samples containing defects having $C_s \in [1, 30]$ Å^2 are shown in Fig. 6 for ion-crater distance of $r \approx 8$ Å, and in Fig. 7 for ion-crater distance of $r \approx 50$ Å. For still larger distances the amount of these centrosymmetry defects is decreased even further.

The planes with normals in the (111) direction in Figs. 6 and 7 have centrosymmetry around 8 Å^2. These planes almost always occur as pairs, and form networks reaching the surface. The planes which are bounded by atoms with no further neighbors have $C_s \approx 1-3$ Å^2, whereas atoms at boundaries where planes are joined have $C_s \approx 5$ Å^2. According to the identification recipe by Kelchner et al.,[31] the planes consist of stacking faults, and the boundary atoms are partial dislocations.

Analysis of the coordination Z (the number of nearest neighbors) of the atoms in the stacking fault planes shows that atoms in them have full coordination $Z = 12$ (as expected), but the atoms at the plane borders are undercoordi-
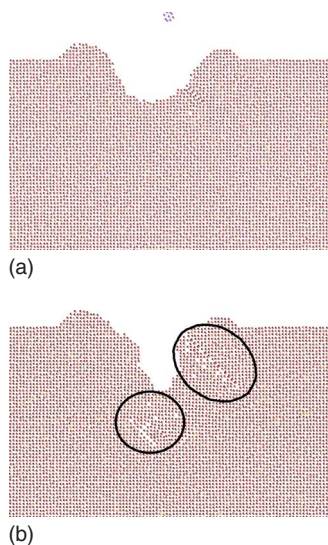
ter. One may also point out the small dip in the curve $f_V(r_i)$ in Fig. 3(a) for $r_i \approx 55$ Å, where the outcome of the bombardment changes from one extended crater to two separate ones. This dip indicates a slight decrease in the total crater volume, which is due to the appearance of a "bridge" that divides the previously connected region into two parts, constituting a new crater and a slightly filled in old crater.

In Fig. 3, displaying the relative change $f_V = (V_1 + V_2)/V_i$ in the total crater volume, a fit of the function

$$f_V(r) = a(1 - e^{-br}) \tag{16}$$

is included. The obtained parameter values are $a = 2.14 \pm 0.03$ and $b = 0.040 \pm 0.002$ Å^{-1}. The parameter a is proportional to the total volume of two separate craters, and b adjusts the volume decrease due to overlapping craters.

FIG. 5. (Color online) (a) Initial and (b) final state of the system when a cluster ion impacts at a distance of $r \approx 8$ Å. Notice the marked defects surrounding the relaxed crater.

nated, with $Z=11$. A visual inspection of a cascade evolution positively identifies the plane borders to be regions of less than normal density. In addition, an analysis of the distance between these border atoms and their closest neighbor reveal that the average value is 2.7 Å, i.e., smaller than the normal nearest-neighbor distance.

From a detailed inspection of the marked regions in Fig. 5 it is seen that two vertical planes (atom columns) are missing between the surface and the low-density marked regions. This observation confirms the result that the centrosymmetry defects are stacking faults and vacancy-type dislocation loops.

C. Sputtering yield

The total sputtering yield as a function of the distance between the initial crater and the cluster ion is shown in Fig. 8. The yield is very small for small ion-crater distances, since the sputtered material must escape from the bottom of the crater. With increasing distance the yield grows, and then seems to stabilize at about 25, when the distance is about twice the radius of the initial crater or larger. The enhanced sputtering for the intermediate distances is due to the fact that material between the impact point and the initial crater is less strongly bound to the bulk than material in a pristine surface—the former material simply has more surrounding surface, including the walls of the initial crater.

The cluster sputtering yield $Y_c = Y_c(N)$ for all the simulations is shown in Fig. 9. The clusters contained between 1 and 95 atoms. The data has been fitted to the function $Y_C(N) = aN^{-b}$, with parameters a and b. Here $Y_c(N)$ is defined as the number of clusters containing N atoms divided by the total number of irradiating atoms, i.e., the total number of simulations times 13. The value of the parameters a,b depend on the lower limit N_{min} of the included data. Parameter values for different limiting values are shown in Table I. The

total sputtering yield was calculated as $Y_s = \Sigma_{N=1}^{N=95} N Y_c(N)$ $= 25 \pm 3$.

The specific choice of the fitting function $Y_c(N)$ is based on experimental results and the so-called Bitensky-Parilis model[34] for sputtering (see Ref. 35 for additional references).

D. Simulation of TEM images

In order to enable comparison of our results with those in the literature we have simulated TEM images of typical relaxed target systems at 300 K. The initial crater is shown in Fig. 10(a), and the final states for ion-crater distances of r $=8$ Å, $r=25$ Å, $r=50$ Å, and $r=75$ Å, are shown in (b)–(e). Simulated TEM images of targets with thickness 74, 132, and 148 Å can be found in (a′)–(e′), (a″)–(e″), and (a‴)–(e‴), respectively. The targets displayed in the last column have the original thickness. All the defects associated with the dislocations (Sec. III B) were situated well inside the target with thickness of 74 Å.

The contrast and brightness of the simulated TEM images varies in a nontrivial way with the thickness of the target, as can be seen from Fig. 10. For targets with the bottom half removed, the crater rims are practically invisible against the black pristine surface, but the craters themselves form distinct white spots. When the thickness is increased, the crater rims become black against a grey pristine surface, but the craters are slightly dimmer. The crater rims on the full-size targets remain black, the pristine surface is slightly brighter than before, and the craters have turned from white to grey.

From the last two rows and the last column in Fig. 10 it is clear that for the thickest target it seems that the initial crater has "melted" into the contrast of the background. This clearly gives the misleading result that the cluster ion has annihilated the initial crater while forming a new one.

The region around the initial impact points in Fig. 10 has a depth of $d=28$ Å. The region around the new impact points have the following depths: (b) $d_1=39$ Å, (c) $d_2=34$ Å, (d) $d_3=28$ Å, and (e) $d_4=28$ Å. In part (b) the electrons can travel a larger distance without scattering or being absorbed than in the other cases, and this gives the widest bright area in figures (b′) and (b″). In parts (d) and (e) the region around the new impact points is wider than for the initial impact points. This explains why there are more electrons passing through and a wider bright area for the region excavated by the second ion in figures (d′), (d″), (e′), and (e″).

TEM images showing a partial annihilation event observed by Donnelly and Birtcher[3] are reprinted in Fig. 11. In this case the crater (made by a 400 keV xenon ion) had a radius of approximately 37 Å. The distance between the crater and the ion is unknown. The illustrated event is consistent with a nearby ion impact, leading to deposition of material into the preexisting crater, but no formation of a second crater, as reported by Donnelly and Birtcher. This can be compared to the present results in Fig. 10 (d‴) and (e‴), where the second cluster ion have seemingly filled in the initial crater. In reality much of the initial crater still remains, as seen in the (d) part.
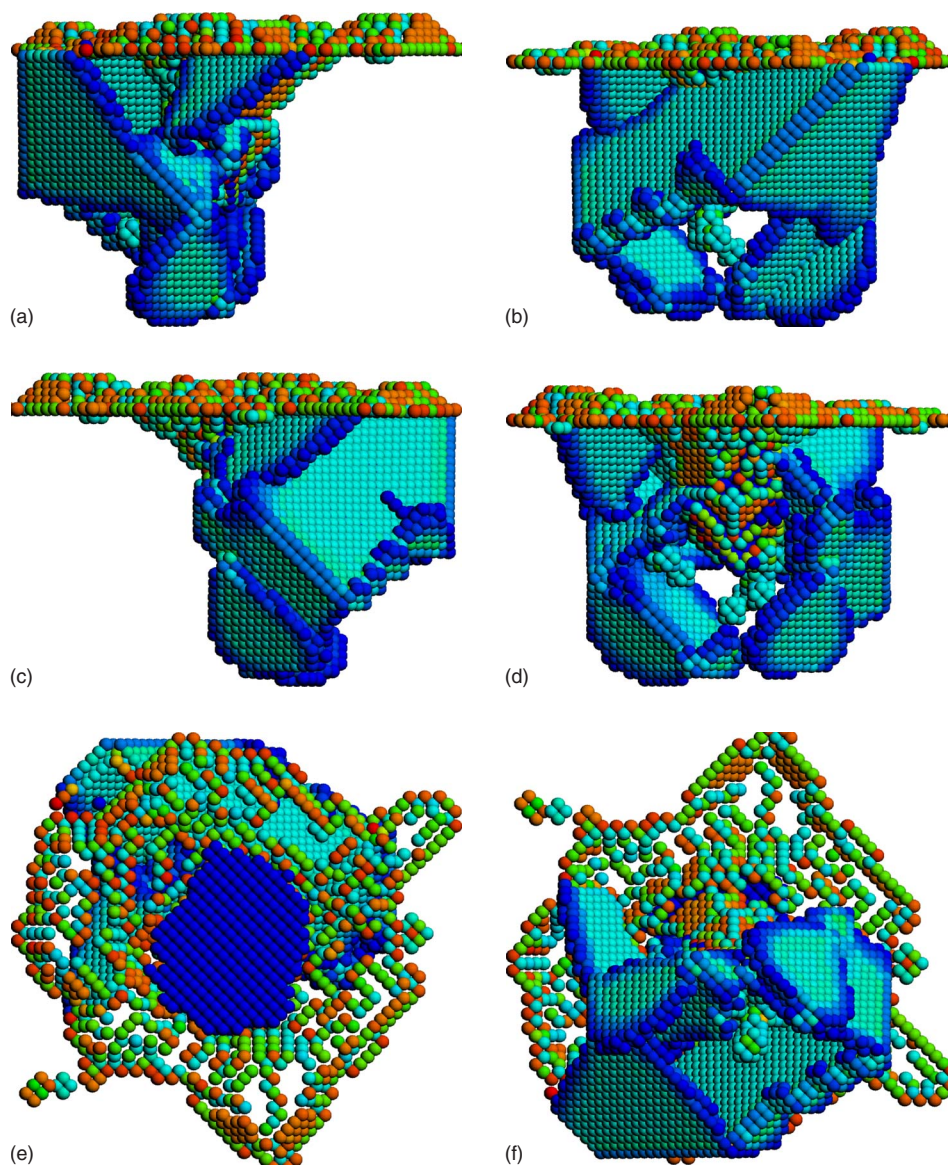
FIG. 6. (Color online) Illustration of defects according to centrosymmetry value when the ion-crater distance was $r \approx 8$ Å. From left to right, row for row: Views of the defects, when the system is rotated anticlockwise around the vertical at each step. The last row shows the view from the top, and the view from the bottom. The craters are dark blue. Colors: Dark blue for $C_s \approx 1-3$ Å^2 and the craters, turquoise for $C_s \approx 10$ Å^2, green for $C_S \approx 20$ Å^2, and orange-red for $C_S \approx 25$ Å^2. The images are centered on the impact point of the cluster ion.

E. Comparison of potential-dependent results

In Table II results for the same distances r and r_i but different potentials—EAM and MC/MC-CEM—are compared. The EAM potential overestimates the growth in total volume: f_V for EAM is at most 64% larger than the corresponding value for MD/MC-CEM. This occurs when $r \approx 8$ Å. The degree of overestimation decreases when r increases, and is minimal for $r \approx 50$ Å, after which it increases slightly.

The values $f_V > 2.2$ in the table are explained by the fact that the initial crater was made using the MD/MC-CEM potential. If the EAM potential had been used the f_V values would be much closer to $f_V = 2.0$.

The relative size of the old crater f grows with increasing radial distance, as expected. When $r \approx 75$ Å the initial crater becomes partly filled-in, as indicated by the negative f values. For this case f should equal $-f_r$, but due to small counting uncertainties there is a very small difference of at most 0.02.

The sputtering yield is larger when the EAM potential is used, and is at most 3.7 times the yield when the MD/MC-CEM potential is used. The general trend for increasing distances is the same as in Fig. 8.

IV. DISCUSSION

A. Growth and annihilation

Experimental results by Donnelly and Birtcher[2,3] show that $50-400$ keV xenon ions incident on gold give rise to craters as well as destroy earlier ones. With the assumption
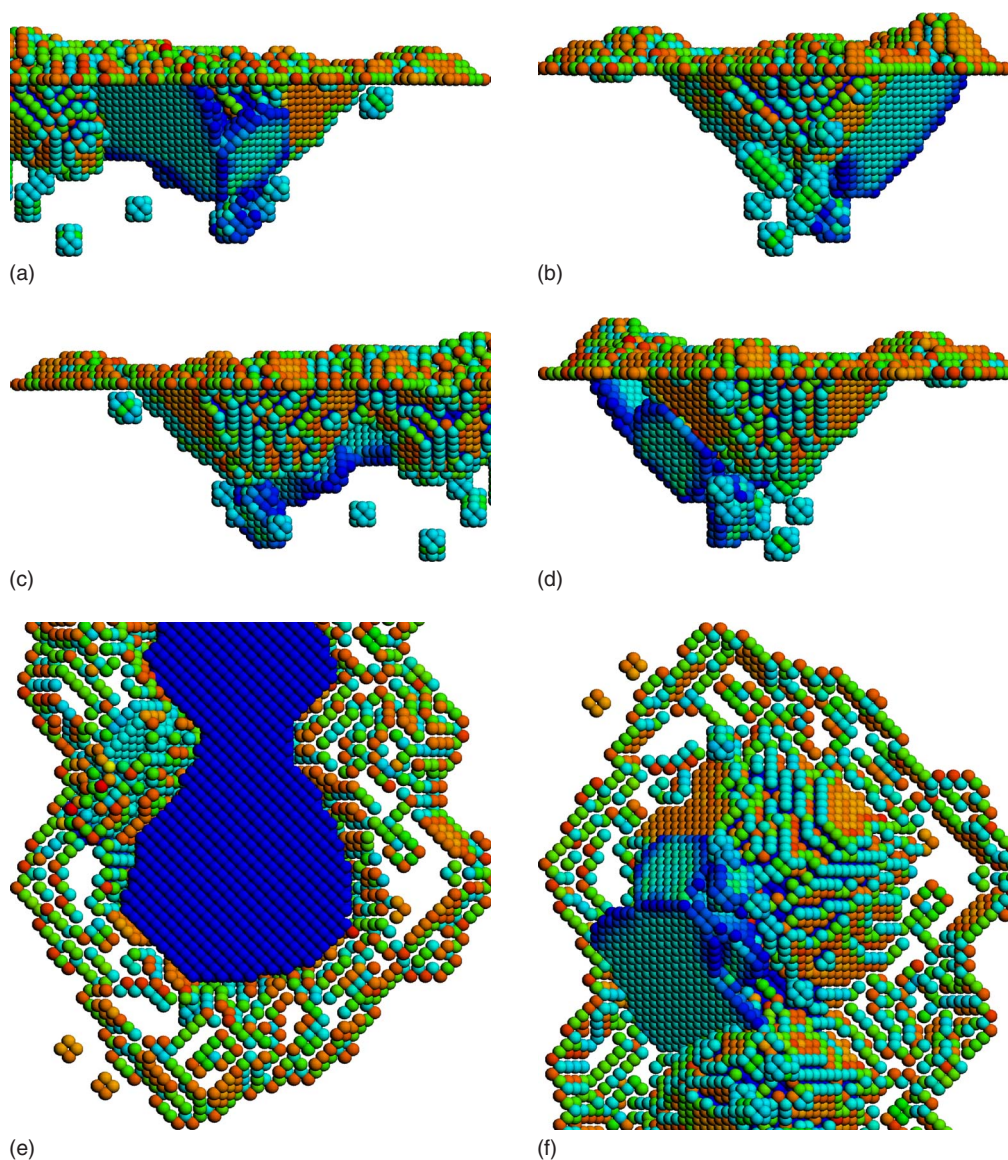
FIG. 7. (Color online) As in Fig. 6 but for an ion-crater distance of $r \approx 50$ Å.

that all ions are capable of annihilating craters, Donnelly and Birtcher[3] conclude from an analysis of TEM images that a single xenon ion had an annihilation cross section of $\sigma_a \approx 85$ nm^2 for small craters with a radius of R of 22 Å. This can be interpreted to mean that an ion impacting within a distance of about 50 Å of a small crater will annihilate this crater, according to the authors. The distance 50 Å corresponds to $R_c = 2.3R$. In the present study $R \approx 28$ Å, so this limit corresponds to $R_c \approx 64$ Å. The interpretation of $f_r = 1$ (full annihilation) for $r < 64$ Å in the study by Donnelly and Birtcher[3] has been indicated in Fig. 4.

The present results show that a 20 keV Ag$_{13}$ ion is unable to destroy a preexisting crater on a (001) silver surface, even when the distance between the crater and the ion is about 8 Å, which is somewhat more than twice the diameter of the cluster ion. The largest filling-in is achieved for a ion-crater distance of about twice the radius of the initial crater. In this case $f_r \approx 0.5$, i.e., half the initial crater is filled-in or removed. The value for f_r decreases when r is increased, as

can be seen in Fig. 4, and drops at $r \approx 70$ Å to about $f_r \approx 0.1$. The agreement with the experimental results of f_r dropping to about zero at $r \approx 64$ Å is noteworthy.

The general discrepancy of more effective crater annihilation in experiments[3] has at least two possible explanations. First, the detection of filling was made using TEM images. Atomic resolution was not obtained, so it is possible that the amount of filling was only 50%, for instance, or some other figure consistent with the TEM images. Second, the perhaps most important filling-in mechanism in hot cascades—flow of molten material—might have been extensive in the experiment, which used higher ion energies and different ion-target combination. For instance, a high surface energy density would lead to more sputtering than liquid flow on the surface. In the experiments 50–400 keV xenon ions would deposit $S(1,E) = 4.7 - 6.6$ keV/nm at the surface,[36] whereas in the present study the corresponding value would be $S(N,E) \approx NS(1,E/N) = 13.6$ keV/nm, where $N = 13$ is the number of atoms in the Ag$_{13}$ cluster ion and $E = 20$ keV is its
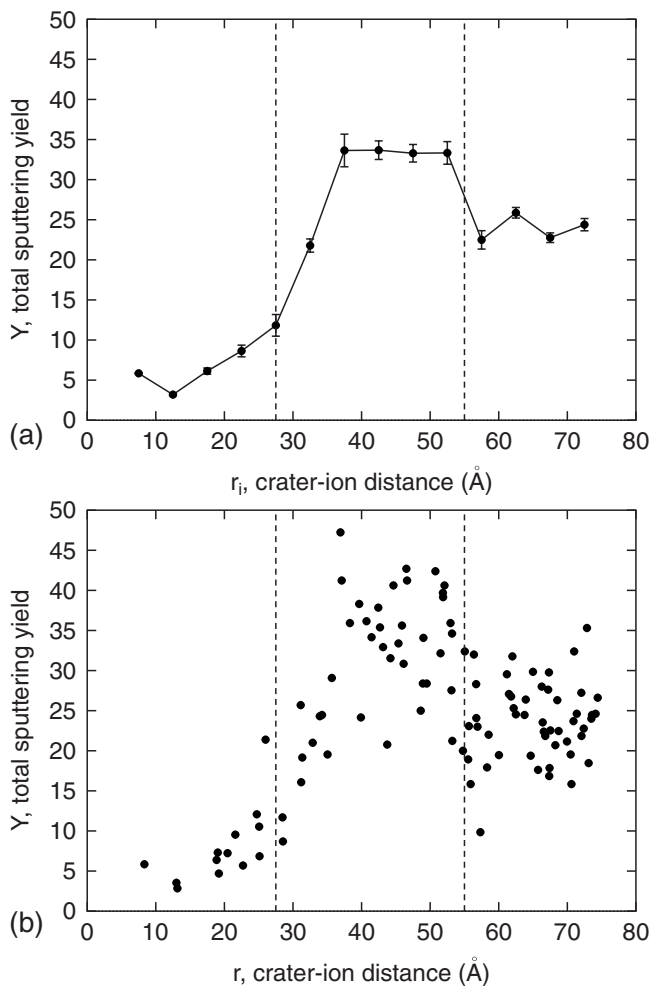
FIG. 8. Results for the total sputtering yield Y, as a function of the (a) binned distance r_i and (b) the real distance r. The broken line is intended as a guide for the eye.

kinetic energy. This assumption of linear scaling is valid for at least gold cluster ions Au_n—with $n=1$, 2, 3, and 7—incident on silicon, aluminum, and copper, with energies
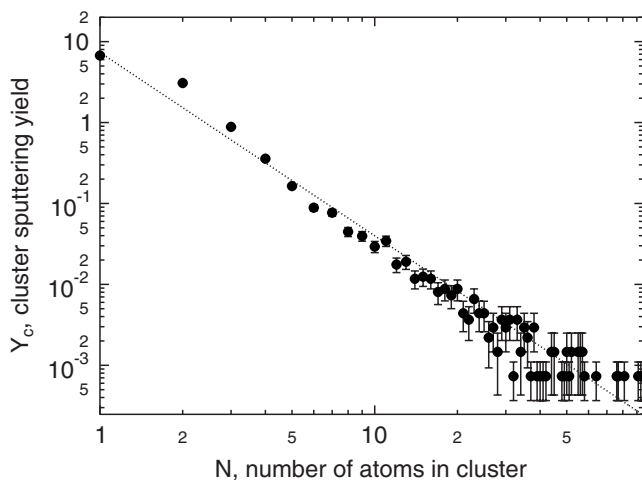

FIG. 9. Total cluster sputtering yield. The line is a fit of the function $Y_c(N)=aN^{-b}$ to data, with parameters a and b. The largest cluster contained 95 atoms.

TABLE I. The dependence of the fit parameters a and b in $Y_c(N)=aN^{-b}$ on the included smallest cluster.

Limit N_{min}	Parameter a	Parameter b
1	7.36±0.07	2.27±0.01
2	23.0±0.7	2.94±0.03
3	16.1±1.0	2.73±0.04
4	10.4±0.9	2.53±0.04
5	7.6±0.9	2.41±0.05
10	10±3	2.50±0.11
15	9±6	2.5±0.2
20	0.2±0.2	1.4±0.3

between 10 keV/atom and $\approx$40keV/atom, as shown by other authors (see references in Ref. 37). By the above arguments, the kinetic energy density deposition in the present study was at least twice the one occurring in the experiments by Donnelly and Birtcher,[3] and would therefore produce less liquid flow, as indicated by the cascade snapshots in Fig. 1.

It should be noted that electrostatic contributions to the energy deposition occurring in the experiments are not included in this comparison. To account for this effect we can use the following arguments. The singly charged xenon ion impinging on the experimental gold target can be considered a point charge incident on a perfect planar conductor. The image charge technique[38,39] can then be used. The increase in kinetic energy of the ion due to the attraction of the image charge is

$$\Delta E = -\frac{e^2}{4\pi\varepsilon_0}\int_a^b dz/(4z^2) = \frac{e^2}{16\pi\varepsilon_0}(1/b - 1/a), \quad (17)$$

where a is the initial distance of the ion from the target and b is the distance at which instantenous charge transfer from target to ion can be considered to take place. According to the classical over-the-barrier model[40,41] this latter distance can be given as

$$b = \sqrt{8Q+2}/(2W), \quad (18)$$

where the ionic charge state is $Q=1$ and W is the work function of the target. There is no dependence on the species or the initial kinetic energy of the ion in Eqs. (17) and (18). In the case of, e.g., the transition metals silver, aluminum, gold, copper, iron, molybdenum, palladium, platinum, and tungsten the work functions for a (001) or a polycrystalline surface are between 4.2 and 5.6 eV (Ref. 42). The corresponding charge transfer distances are 4.0–5.4 Å, resulting in kinetic energy contributions $\lesssim$1 eV, which are insensitive to the initial distance $a \geq 1$ mm between the ion and the target. This energy change is insignificant, since the initial energy of the ions was 50–400 keV in the experiments by Donelly and Birtcher.[3]

The good fit of the (r, f_V) data to the simple model in Eq. (16) is remarkable. However, the physical meaning of this particular model is not obvious. The convenient expression Eq. (16) has the required property that it tends to 2.0 when $r \rightarrow \infty$, representing the formation of two separate and
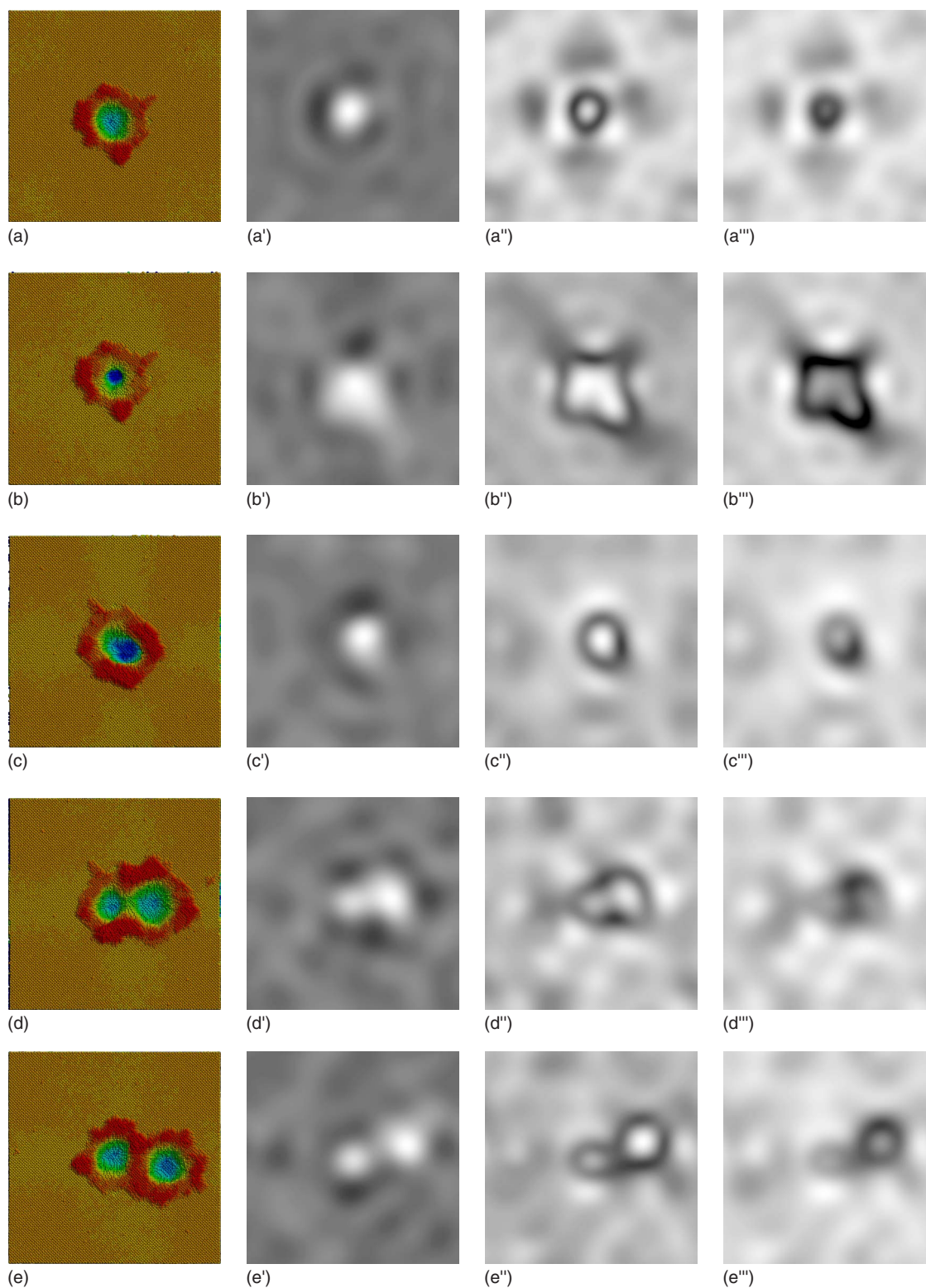
FIG. 10. (Color online) Atomic images of (a) the initial crater and final states for ion-crater distances of (b) $r=8$ Å, (c) $r=25$ Å, (d) $r=50$ Å, and (e) $r=75$ Å. TEM simulated images of targets thinned from the open unirradiated bottom surface are shown in the two innermost columns. These targets have thicknesses of (a′)–(e′) 74 Å and (a″)–(e″) 132 Å. The last column shows TEM images of the un-thinned targets, with a thickness of 148 Å. All the images are centered on the initial crater.

equally large craters when the ion-crater distance is increased. However, the trend in the (r, f_V) data might be explained equally well by some other more complicated model that have a stronger physical motivation.

B. Dislocations

The dislocations—the borders of the (111) planes—observed in Figs. 6 and 7 have also been found in 10 and
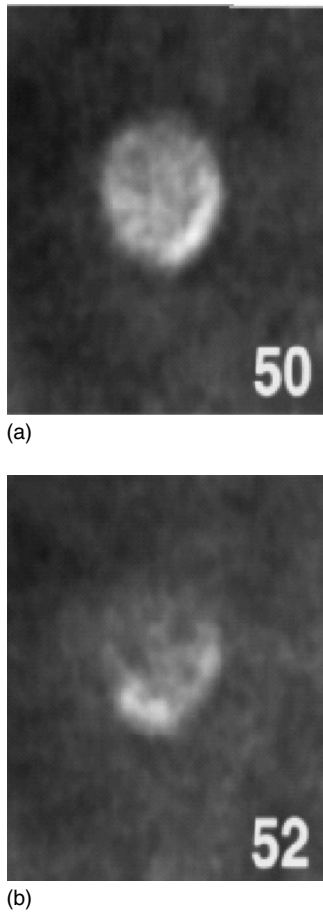
(a)

(b)

FIG. 11. TEM images illustrating a partial annihilation event of a crater with radius of about 37 Å by a 400 keV xenon ion. The numbers in white indicate video frame numbers. Adapted with permission from Ref. 3. Copyright 1997 by the American Physical Society.

20 keV self-bombardment of gold investigated using the EAM potential.[5] In this case the dislocations were made visible by plotting atoms with an energy over a certain threshold, not by investigating the centrosymmetry. It is interesting to note that similar networks of stacking faults and dislocations have also been observed in studies of nanoindentation,[31,32] even though the initial high pressure in this case is produced at time scales that are orders of magnitudes larger.

C. Sputtering yield

The fitted exponents b in Sec. III C are between 2 and 3 when most clusters are included in the fit. In comparison, experiments on silver,[43] indium,[44] and gold[45]—as well as MD simulations of silver[35,46,47] and gold[35,48]—give values of b between the same limits. The Bitensky-Parilis model mentioned in Sec. III C predicts asymptotic exponents (when excluding "small" clusters) of about 1.7 or 2.3. The present results are in other words in very good agreement with experiments and theory.

TABLE II. Growth factor f, relative change in total crater volume f_V, removal factor f_r, and total sputtering yield Y for initially identical systems simulated with the EAM and MD/MC-CEM potentials.

Potential	Cascade	r (Å)	f	f_V	f_r	Y
EAM	A	≈ 8	0.13	1.13	0.42	19
	B	≈ 25	0.99	1.99	0.18	30
	C	≈ 50	1.25	2.25	0.21	67
	D	≈ 75	−0.09	2.38	0.10	46
MD/MC-CEM	A	≈ 8	−0.31	0.69	0.45	6
	B	≈ 25	0.49	1.49	0.26	12
	C	≈ 50	1.11	2.11	0.22	35
	D	≈ 75	−0.05	2.21	0.07	27

D. Simulation of TEM images

As mentioned in Sec. IV D the TEM simulated targets had thicknesses of about 7, 13, and 15 nm in the direction of the electron beam. In comparison, the TEM images in the experimental studies of crater annihilation by Donnelly and Birtcher[2,3] are based on targets with thicknesses of about 20–50 nm (assumed)[2] and 60 nm (Ref. 3). This latter value is four times larger than the thickest sample used in the present study. From Figs. 10(d′)–10(d‴), and especially Figs. 10(e′)–10(e‴), it is clear that the thickening of the sample by a factor of two has lead to almost full extinction of the spot representing the initial crater, giving the misleading result that the initial crater has been filled in. However, the notion that weaker spots weaken and disappear with increasing thickness of the target—as shown above—is not true in general.

The nontrivial dependence of the intensity and the contrast on the thickness of the sample (and the defocus of the objective lens) in TEM studies has been pointed out by, e.g., Diebold et al.[49] When using TEM, the whole of the sample is illuminated at the same time, and a resulting real-space image is therefore made up of transmitted and diffracted electron beams. Atoms and other details in the sample may then correspond to minima, maxima, or other values of the intensity, depending on sample thickness and defocus. In comparison, the interpretation of scanning transmission electron microscopy (STEM) images is more straightforward, since these images are formed by scanning the electron beam across the sample point by point and measuring the transmitted intensity. In this case large intensities indicate holes or voids in the sample, whereas low intensities correspond to atomic columns.

The present finding that the spot corresponding to the initial crater tends to vanish when the thickness of the target is increased may be put into question with regards to the complications mentioned above. Specifically, there are no guarantees that this conclusion holds for targets even thicker than those used here—the weakened spots may perhaps increase in brightness for some specific thickness values. In any case, the simulated images in this study verify the generally complicated dependence of TEM images on experimental parameters such as target thickness.

E. Comparison of potential-dependent results

The results in Table II show that $f_V = (V_1 + V_2)/V_i$ and Y are without exception larger when the EAM potential is used. This means that more atoms are excavated and sputtered—and more vacancies are formed—in this case. Similar results of "over-sputtering" has been reported earlier for gold.[10] The basic explanation for excessive sputtering and displacement of atoms is most likely due to too small surface energies[20,24] and melting temperatures T_m of EAM potentials over MD/MC-CEM potentials. For silver the EAM potential gives $T_m = 1150$ K, whereas the MD/MC-CEM potential gives $T_m = 1325$ K, a value which is 1.2 times larger. These melting temperatures were calculated by simulating solid and liquid phases in equilibrium.

V. CONCLUSIONS

The impacts of silver cluster ions with 13 atoms and a total energy of 20 keV with silver surfaces with a preexisting crater have been examined using molecular dynamics computer simulations. The results show that the impacts are largely unable to fully annihilate pre-existing craters on a silver (001) surface. Simulation of TEM images of the damaged targets indicates that experimental findings of annihilation based on TEM images may be misleading, as partially annihilated craters may be invisible in the TEM. Also, the lattice damage created below the craters by the cluster ions is similar to the damage observed during nanoindentation. Furthermore, the distribution of clusters in the sputtered material agrees with experiments and other theoretical studies.

*krihen@kth.se

[1] K. L. Merkle and W. Jäger, Philos. Mag. A **44**, 741 (1981).

[2] R. C. Birtcher and S. E. Donnelly, Phys. Rev. Lett. **77**, 4374 (1996).

[3] S. E. Donnelly and R. C. Birtcher, Phys. Rev. B **56**, 13599 (1997).

[4] R. C. Birtcher and S. E. Donnelly, Mater. Chem. Phys. **54**, 111 (1998).

[5] M. Ghaly and R. S. Averback, Phys. Rev. Lett. **72**, 364 (1994).

[6] T. J. Colla, R. Aderjan, R. Kissel, and H. M. Urbassek, Phys. Rev. B **62**, 8487 (2000).

[7] R. Aderjan and H. M. Urbassek, Nucl. Instrum. Methods Phys. Res. B **164-165**, 697 (2000).

[8] E. M. Bringa, K. Nordlund, and J. Keinonen, Phys. Rev. B **64**, 235426 (2001).

[9] K. Nordlund, K. O. E. Henriksson, and J. Keinonen, Appl. Phys. Lett. **79**, 3624 (2001).

[10] J. Samela, J. Kotakoski, K. Nordlund, and J. Keinonen, Nucl. Instrum. Methods Phys. Res. B **239**, 331 (2005).

[11] K. O. E. Henriksson, K. Nordlund, and J. Keinonen, Nucl. Instrum. Methods Phys. Res. B **255**, 259 (2007).

[12] T. J. Colla and H. M. Urbassek, Nucl. Instrum. Methods Phys. Res. B **164-165**, 687 (2000).

[13] G. W. Gear, *Numerical Initial Value Problems in Ordinary Differential Equations* (Prentice-Hall, Englewood Cliffs, NJ, USA, 1971).

[14] K. Nordlund, Comput. Mater. Sci. **3**, 448 (1995).

[15] M. P. Allen and D. J. Tildesley, *Computer Simulation of Liquids* (Oxford University Press, Oxford, UK, 1989), and references therein.

[16] J. D. Kress and A. E. DePristo, J. Chem. Phys. **87**, 4700 (1987).

[17] J. D. Kress and A. E. DePristo, J. Chem. Phys. **88**, 2596 (1988).

[18] J. D. Kress, M. S. Stave, and A. E. DePristo, J. Phys. Chem. **93**, 1556 (1989).

[19] T. J. Raeker and A. E. DePristo, Phys. Rev. B **39**, 9967 (1989).

[20] M. S. Stave, D. E. Sanders, T. J. Raeker, and A. E. DePristo, J. Chem. Phys. **93**, 4413 (1990).

[21] C. Kelchner, D. Halstead, L. Perkins, N. Wallace, and A. DePristo, Surf. Sci. **310**, 425 (1994), and references therein.

[22] M. S. Daw and M. I. Baskes, Phys. Rev. Lett. **50**, 1285 (1983).

[23] M. S. Daw and M. I. Baskes, Phys. Rev. B **29**, 6443 (1984).

[24] S. M. Foiles, M. I. Baskes, and M. S. Daw, Phys. Rev. B **33**, 7983 (1986).

[25] M. S. Daw, Phys. Rev. B **39**, 7441 (1989).

[26] M. S. Daw, S. M. Foiles, and M. I. Baskes, Mater. Sci. Rep. **9**, 251 (1993).

[27] S. B. Sinnott, M. S. Stave, T. J. Raeker, and A. E. DePristo, Phys. Rev. B **44**, 8927 (1991).

[28] A. Wucher and B. Garrison, J. Chem. Phys. **105**, 5999 (1996).

[29] J. F. Ziegler, J. P. Biersack, and U. Littmark, *The Stopping and Range of Ions in Matter* (Pergamon, New York, 1985).

[30] H. J. C. Berendsen, J. P. M. Postma, W. F. van Gunsteren, A. D. Nola, and J. R. Haak, J. Chem. Phys. **81**, 3684 (1984).

[31] C. L. Kelchner, S. J. Plimpton, and J. C. Hamilton, Phys. Rev. B **58**, 11085 (1998).

[32] J. Knap and M. Ortiz, Phys. Rev. Lett. **90**, 226102 (2003).

[33] E. J. Kirkland, *Advanced Computing in Electron Microscopy* (Kluwer, Dordrecht, 1998).

[34] I. S. Bitensky and E. S. Parilis, Nucl. Instrum. Methods Phys. Res. B **21**, 26 (1987), and references therein.

[35] K. O. E. Henriksson, K. Nordlund, and J. Keinonen, Phys. Rev. B **71**, 014117 (2005).

[36] J. P. Biersack and L. G. Haggmark, Nucl. Instrum. Methods **174**, 257 (1980).

[37] S. Bouneau, A. Brunelle, S. Della-Negra, J. Depauw, D. Jacquet, Y. LeBeyec, M. Pautrat, M. Fallavier, J. C. Poizat, and H. H.

Andersen, Phys. Rev. B **65**, 144106 (2002).

[38] J. R. Reitz, F. J. Milford, and R. W. Christy, *Foundations of Electromagnetic Theory* (Addison-Wesley, New York, 1992).

[39] J. D. Jackson, *Classical Electrodynamics* (Wiley, New York, 1998).

[40] J. Burgdörfer, P. Lerner, and F. W. Meyer, Phys. Rev. A **44**, 5674 (1991).

[41] C. Lemell, H. P. Winter, F. Aumayr, J. Burgdörfer, and F. Meyer, Phys. Rev. A **53**, 880 (1996).

[42] D. R. Lide, *CRC Handbook of Chemistry and Physics*, 82nd ed. (CRC Press LLC, Boca Raton, FL, 2001).

[43] C. Staudt, R. Heinrich, and A. Wucher, Nucl. Instrum. Methods Phys. Res. B **164-165**, 677 (2000).

[44] C. Staudt and A. Wucher, Phys. Rev. B **66**, 075419 (2002).

[45] L. E. Rehn, R. C. Birtcher, S. E. Donnelly, P. M. Baldo, and L. Funk, Phys. Rev. Lett. **87**, 207601 (2001).

[46] A. Wucher, Nucl. Instrum. Methods Phys. Res. B **83**, 79 (1993).

[47] M. Lindenblatt, R. Heinrich, A. Wucher, and B. Garrison, J. Chem. Phys. **115**, 8643 (2001).

[48] R. Kissel and H. M. Urbassek, Nucl. Instrum. Methods Phys. Res. B **180**, 293 (2001).

[49] A. C. Diebold, B. Foran, C. Kisielowski, D. A. Muller, S. J. Pennycook, E. Principe, and S. Stemmer, Microsc. Microanal. Microstruct. **9**, 493 (2003).